DALLAS SEMICONDUCTOR MAXIM
Engineering Journal
Volume Forty-Seven

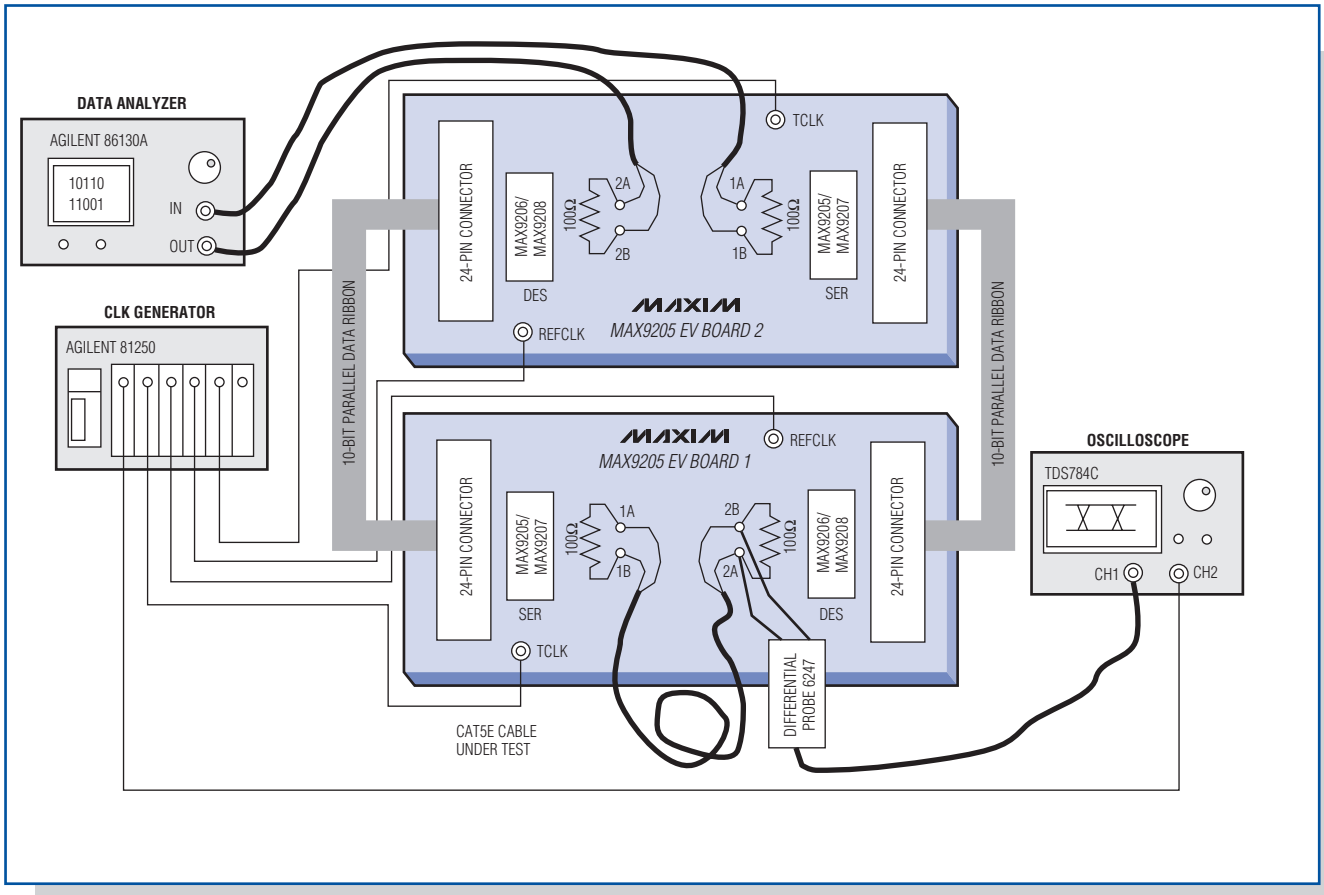

The MAX9205 EV kit's serializer-deserializer cable test setup is used to convert the serial I/O to parallel I/O. (See article inside, page 7.)

MAXIM REPORTS REVENUES AND EARNINGS FOR THE SECOND QUARTER OF FISCAL 2003

Maxim Integrated Products, Inc., (MXIM) reported net revenues of $286.1 million for its fiscal second quarter ending December 28, 2002, an increase over the $247.1 million reported for the second quarter of fiscal 2002 and unchanged from reported revenues for the first quarter of fiscal 2003. Net income for the quarter was $77.1 million, an increase over the $62.6 million reported last year and an increase over the $73.2 million reported for the previous quarter. Diluted earnings per share were $0.23 for the second quarter, an increase over the $0.18 reported for the same period a year ago and up from the $0.22 reported for the first quarter of fiscal 2003.

During the quarter, cash and short-term investments increased $158.0 million to $945.7 million after the Company repurchased 500,000 shares of its common stock for $18.3 million, paid dividends of $6.4 million, and acquired a total of $8.4 million of capital equipment. Accounts receivable decreased by $12.9 million in the second quarter to $122.6 million, and inventories decreased $8.4 million to $127.9 million. Inventories have decreased $19.8 million from third quarter fiscal 2002 levels, and no inventory growth is anticipated for the third quarter of fiscal 2003. Gross margin for the second quarter increased slightly, after increasing inventory reserves $3.0 million, compared to the first quarter.

Second quarter bookings were approximately $271 million, up slightly from the first quarter's level. Turns orders received during the quarter were $139 million, an 8% increase over the $129 million received in the prior quarter (turns orders are customer orders that are for delivery within the same quarter and may result in revenue within the same quarter if the Company has available inventory that matches those orders). Order cancellations continued to be below historical levels. Bookings increased in the Pacific Rim and Europe but decreased in the U.S. and Japan. Second quarter ending backlog shippable within the next 12 months was approximately $201 million, including $177 million requested for shipment in the third quarter of fiscal 2003.

Jack Gifford, Chairman, President, and Chief Executive Officer, commented on the quarter: "Although overall bookings levels were relatively unchanged from last quarter, we were encouraged to see an increase in orders for products such as data converters that target the broad-based industrial market. We continue to hold a cautious view of any significant near-term upturn in the long-haul telecommunications industry, and we have yet to see an improvement in orders for our products addressing that sector. The trend we have seen over the past several quarters, with customers ordering for near-term needs and the resulting high level of turns, continued this quarter. Visibility at our end customers remains limited."

Mr. Gifford continued: "Maxim continues to perform well for its stockholders in a still challenging business environment. Diluted earnings increased 4.5% sequentially on flat revenues and 27.8% year over year on 15.8% revenue growth. While increased efficiency remains a focus, we continue to be highly productive in the new product development area. In our new product quarter ending January 25, 2003, we introduced 427 engineering man months of products, an 18% increase over the same quarter in fiscal 2002."

Mr. Gifford concluded: "The Company's Board of Directors has declared a quarterly cash dividend of $0.02 per share. Payment will be made on February 28, 2003 to stockholders of record on February 10, 2003."

Misconceptions stall adoption of fuel gauging in wireless handsets

Merging wireless communication with data in the newest handsets and PDAs sets the stage for another leap in productivity. With that will come an economic boost and change in our working lifestyle. PC notebooks broke similar ground in portable computing; power loss and the corresponding uncertainty of data loss were concerns, mitigated by the inclusion of smart-battery technology to track usage and predict run-time accurately. Today, most hand-held product manufacturers retreat from accurate battery-monitor electronics. This reluctance is due mainly to several misconceptions regarding accurate battery monitoring; these misconceptions should not, however, delay designers from stepping forward and accepting the challenge. The DS276x and DS277x products accurately monitor usable battery life at all temperatures, rates, and aging conditions, thus enabling hand-held systems to extract the most charge to keep battery sizes small, while reducing the risk of data loss.

Misconception 1: Accurate battery information does not increase the run time.

The increase in memory requirements of wireless handhelds means that application programs and user files are stored in volatile RAM memory. A loss of battery power would destroy files that the user created or purchased. Some systems use rechargeable coin batteries to power the memory when the main battery is empty or disconnected, but even the largest of these cells has only a 25mAh capacity and does not hold the memory longer than 1 day. Typical coin cells, moreover, hold less than 5mAh and are exhausted in a matter of hours. Therefore, data-centric wireless handhelds must be shut down before the main battery is completely discharged, thus ensuring sufficient reserve capacity to preserve the memory contents until a charger is connected. Most users require a battery-usage minimum of 5 days, but prefer 10 days or more. Ideally, the battery used on feature-rich handsets or wireless PDAs should be shut down with 100mAh to 200mAh remaining from its 900mAh to 2000mAh fuel capacity.

As an example, assume an application requires 150mAh reserve capacity. The +20°C curve in Figure 1 shows that choosing a cutoff voltage of 3.5V leaves the appropriate amount of capacity in the cell. However, the 0°C and +40°C curves do not correlate. If the battery is cold (0°C on the curve), the voltage is depressed. Using 3.5V as the cutoff results in over 400mAh for reserve and less than 600mAh for run time. Conversely, when the battery is warm, the voltage is elevated. Less than 100mAh is available for reserve (+40°C on the curve).

Variations in the load current also have a significant effect. The curves in Figure 2 show the voltage profiles resulting from three discharge rates: C/2, C/5, and C/10, where C equals the charge capacity of the cell. This shows that reserve capacity resulting from a 3.5V cutoff varies

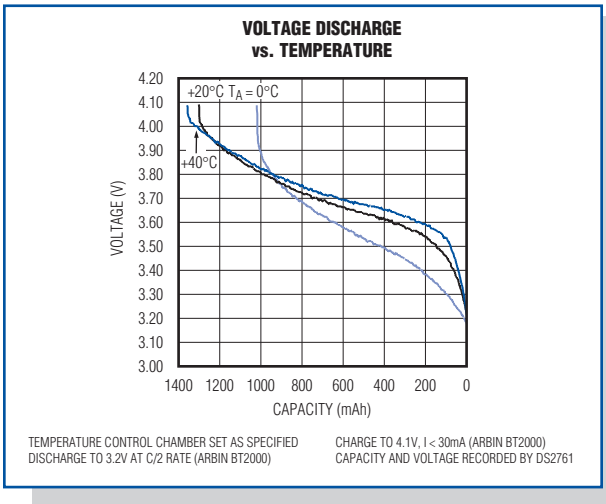

Figure 1. Voltage discharge profile varies with temperature. If the battery is cold, voltage is depressed. If the battery is warm, voltage is elevated.

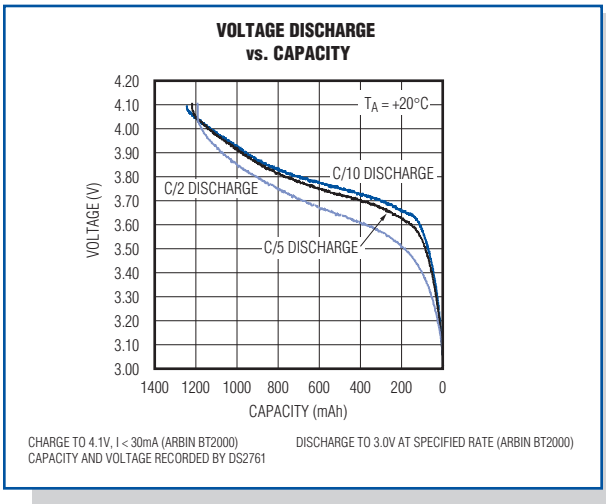

Figure 2. Voltage profile varies with discharge rate. Increasing the cutoff voltage decreases the reserve capacity.

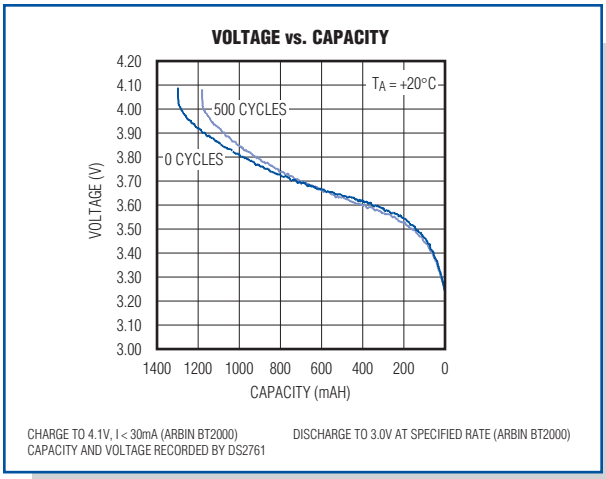

Figure 3. C/2 discharge voltage profile varies with aging. This example shows a particularly good cell performing under this stress.

from <100mAh for C/10 to >200mAh for C/2. Increasing the cutoff voltage to 3.6V to ensure sufficient reserve with a C/10 load condition varies the reserve from 150mAh to 400mAh over the three discharge rates. Thus, trying to increase the reserve capacity by increasing the cutoff voltage brings a large penalty .

Although not as dramatic, the aging of battery cells also changes the voltage profile. Aging varies from cell to cell and significantly by manufacturer. Moreover, subjecting a cell to shallow discharge cycles has a different effect than full discharge cycles. Figure 3 shows that a permanent loss of 150mAh from full battery capacity occurs over 500 cycles. This is an example of a cell performing particularly well under this stress. The effect on reserve capacity is 50mAh to 75mAh, based on aging from repeated full-discharge cycling.

Flawed methods of measuring capacity

Lookup tables can compensate for the wide variation in terminal voltage due to temperature, discharge rate, and aging. However, this method is error prone and also requires measurements for temperature and current. To be accurate, the current and voltage measurements should be taken simultaneously to ensure that the terminal voltage data coincides with the discharge rate. For this reason, many voltage-based capacity implementations are done without consideration of discharge rate. Using voltage and temperature alone requires a two-dimensional lookup table to store nominal cell characteristics for computing an estimate of remaining capacity. This method yields 20% to 40% error across the full temperature range.

Because the voltage-based method suffers from limited accuracy, a common alternate approach employs a larger battery than necessary. This affects the size of the handheld, which is a critical competitive issue for these devices. Yet another alternative uses a small battery with less run time or higher risk of data loss. The optimal choice includes an intelligent battery monitor (such as those in the DS276x and DS277x families), which increases run time without increasing the size of the handheld or increasing the risk of data loss.

How intelligent battery monitors work

Intelligent battery monitors typically avoid the lookup of capacity based on voltage, temperature, and current. Instead, the charge flow into and out of the battery is measured. A coulomb counter tracks the charge stored in the battery. Temperature and discharge rate measurements are used to compensate for the cell's ability to deliver stored charge based on a small lookup table that stores the cell characteristics. The DS276x and DS277x families provide all measurement and data storage necessary, with algorithm storage and result computation provided by the host system. A maximum error of 3% can be expected when discharging from full at temperatures <+15°C. A combined error of 5% is achieved over all temperature, load, and age conditions. If the time between full charges increases beyond 2 weeks, input offset errors become more frequent. However, most users fully charge every week. **Table 1** shows the key features and performance of battery monitors.

Table 1. Battery monitor features and performance

Device	Measured Parameters*	Current Range (mV)	Current Offset (µV)	Data Storage	Other Features
DS2761	V, T, I	±64	±15	32 bytes EEPROM	Li+ protector
DS2770	V, T, I	±51	±1.6	40 bytes EEPROM	Li+/NiMH charger

*V = Voltage, T = Temperature, I = Time

Misconception 2: Displaying accurate battery information does not benefit users.

It is a common belief among manufacturers that users do not appreciate or are confused by a battery capacity display beyond a few bars or the simplistic image of a battery with three diagonal slices. Many manufacturers believe users are satisfied with simple bar displays that are too coarse to show the real changes in run time. While perhaps true for some voice-only cellular users, this is not true of full-featured, wireless data device users. The latter users are migrating from notebook PCs and are accustomed to a numerical percentage display of available capacity, predicted run time, standby, and charge times.

Some manufacturers are reluctant to display predictive battery capacity data because any assessment of available run or talk time is based on current usage conditions. They cannot factor in changing conditions before they occur. Equipment makers also want to avoid disappointing customers by predicting the wrong run time because the user changed from a low-consumption to a high-consumption mode.

The user base for wireless data devices should not, however, be underestimated. Most are quite familiar with the difference between usage modes, just as they understand that cars get more miles per tank on the highway than in the city, or with a light load vs. a full load. Nor are users confused by changes in run time when they run downloaded third-party software or CompactFlash® add-in hardware on today's hand-held systems.

Battery uncertainty is especially true for the charge in the lower half of the battery. How much battery life really remains in handhelds when all you see is the common three- or four-segment battery display? Because of dropped calls, interrupted data exchange, and lost data files, experience has taught users not to trust the data display. Consequently, some users charge their handhelds when one or two segments of the battery display are gone. With poor accuracy and too few battery display segments, users might revert to more wired transactions. How many wireless data transactions are avoided because the user wants to save the battery power for an emergency voice call later? But intelligent battery monitors display estimated run time, so users are aware of different power consumption modes. The quantitative power estimate of the DS276x and DS277x allows users to choose how to consume the energy stored in each battery charge.

Misconception 3: The battery monitor needs to be accurate in standby mode for several months.

This is an issue with the deployment of batteries in new equipment. Batteries are usually shipped from the factory 3 to 9 months before reaching the end user. With the offset performance of battery monitors in the 1.6mV to 30mV range, small offset errors accumulated over several months (thousands of hours) equate to a large percentage of consumed battery capacity. Manufacturers are concerned that the monitor may indicate a dead or full battery, when in reality the capacity is approximately 30%. Until offset errors can be tamed to the submicrovolt range, this situation will persist.

The battery should be fully charged by the user before use. The first full charge is an important step that "forms" the cell and is highly recommended for optimal battery performance. A clear disclaimer in the owner's manual directs customers to fully charge the battery before initial use. A full charge is often recommended if the battery has not been used for several months. Whenever the battery is fully charged, the battery monitor's coulomb count—the accumulated current register (ACR) on the DS276x and DS277x series devices—can be synchronized with the cell.

Misconception 4: Intelligent battery monitoring adds too much cost.

When the first battery monitor solutions reached market, wireless communication served voice-only handsets. PDAs connected through PCs on short-range infrared or serial links. Bluetooth™, Wi-Fi®, and 3G network technologies were under development. An intelligent battery monitor was neither cost effective nor essential.

Because data is now both valuable and vulnerable, situations have changed. Intelligent battery monitors increase run time, enable development of smaller devices, add value to the user's experience, and encourage more wireless activity. When a user spends between $200 and $600 on a wireless hand-held data device and an additional $40 to $100 per month on service fees, what is the value of increased operating time that is accurately displayed? For the hand-held manufacturer competing on size, performance, and cost, is it worth the ability to shrink the newest model? For the wireless operators trying to increase subscriber use of data services, how do you value

CompactFlash is a registered trademark of CompactFlash Association.
Bluetooth is a trademark of Bluetooth SIG, Inc.
Wi-Fi is a registered trademark of the Wi-Fi Alliance.

user confidence that the battery is not rapidly depleted? Only a few industry leaders understand that the value of intelligent battery monitoring far exceeds its cost. Right now, those products outpace the competition in run time and user satisfaction. So, in that sense, they are reaping a reward, not paying a price.

Conclusion

Revolutionary product features often evolve from "nice-to-have" bonus properties to "must-have" core or enabling features. Intelligent battery monitoring is such a feature. With the move to hand-held computing and communications increasing, users will not tolerate an unpredictable estimation of battery capacity represented by only a few visual battery segments. As long as voltage-based solutions prevail, so will larger batteries, larger handhelds, early shutdowns, and low user confidence. Fortunately, however, predicting battery power is now quite reliable. Intelligent battery monitors such as the DS276x and DS277x product lines enable wireless handhelds to evolve like PCs, decreasing size while increasing performance and user confidence.

LVDS serializer-deserializer performance over twisted-pair cable

A serializer-deserializer pair reduces interconnect wiring in applications requiring high-bandwidth data communications over short distances such as in telecom and networking equipment backplanes, intrarack connections for 3G cell-phone base stations, and digital video interfaces. Advantages of current-mode, low-voltage differential signaling (LVDS) include simplified termination, low transmission power, and low electromagnetic interference (EMI). The main LVDS standard, TIA/EIA-644-A, specifies physical layer parameters such as signal levels, but does not specify interconnect performance such as data rate vs. cable length. The LVDS standard offers users the basic compatibility of LVDS signaling, but must be supplemented in high data-rate applications with information on attainable performance with a given cable type and length.

Maxim's MAX9205/MAX9207 LVDS serializers and MAX9206/MAX9208 LVDS deserializers transmit high-speed data over a serial point-to-point link with 100Ω differential characteristic impedance. The serial "payload" data rate (with overhead synchronization bits excluded) is 160Mbps to 400Mbps for the MAX9205/MAX9206 pair and 400Mbps to 600Mbps for the MAX9207/MAX9208 pair. Both pairs have the same pinout, but each is optimized for a different frequency range.

This article presents laboratory test results and analysis of the bit-error ratio (BER) performance of the MAX9205/MAX9207 LVDS serializers and the MAX9206/MAX9208 deserializers at different data rates and cable lengths. This article also correlates BER with the jitter measured on link eye diagrams using unshielded twisted-pair CAT-5E cable of various lengths. System designers should gain a better understanding of the Maxim devices and their application.

BER test

The BER test is the most straightforward and accurate way to measure the reliability of a link. Digital communication links require very low error ratios—on the order of one error in 100 billion received bits (BER of 10^{-12}) or less.

To perform a BER test, however, a high-performance signal generator and specialized test equipment are needed. The BER test, depending on the transmission rate, can take hours or even days to transfer the number of bits required to test for a BER of 10^{-12} or less. Due to the time-consuming nature of a BER test, faster measures are commonly employed to predict link reliability, such as establishing jitter levels that produce a low BER. Jitter for the MAX9205/MAX9206 and MAX9207/MAX9208 links is measured and correlated to BER. The BER test is used to validate the data sheet jitter maximum values. **Figure 1** shows a configuration of a point-to-point link established on an LVDS serializer/deserializer.

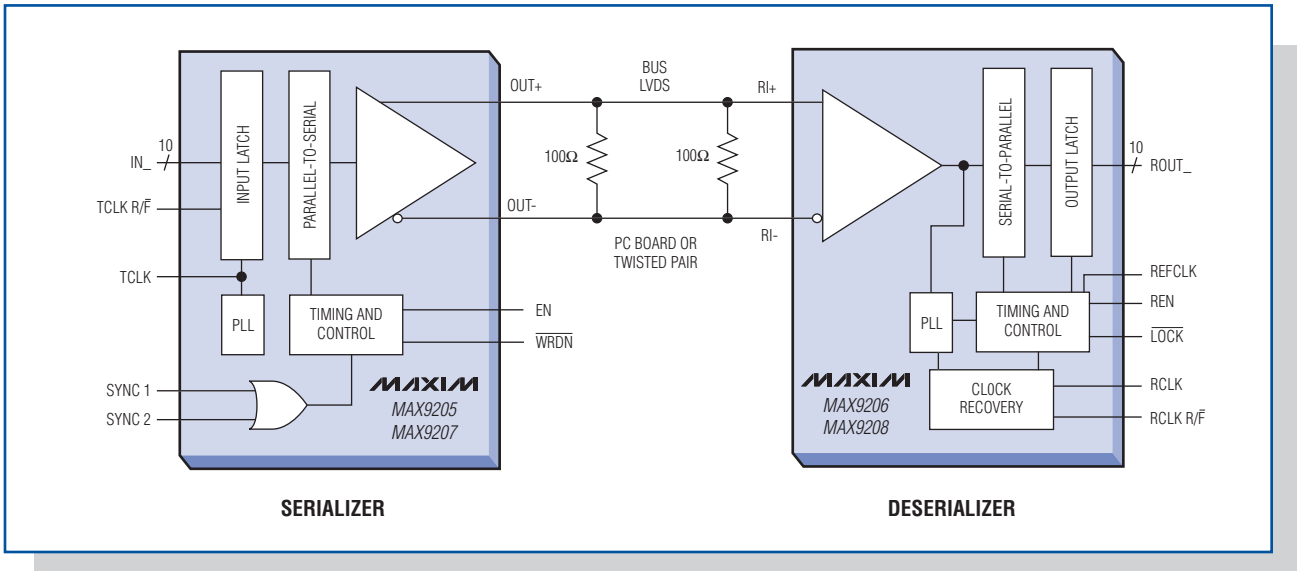

Figure 1. These diagrams show a point-to-point link with a serializer/deserializer.

Test setup

The MAX9205 or MAX9207 LVDS serializer transmits the LVDS signal. The serializer latches 10 bits of parallel data on the rising edge of the parallel data clock (TCLK), adds 2 overhead synchronization bits, and transmits the serialized data through a single LVDS output. The parallel data clock range is 16MHz to 40MHz for the MAX9205 and 40MHz to 60MHz for the MAX9207. With the 2 synchronization bits included, the serial bit rate is 12 x TCLK. The "payload" serial data rate (serial bit rate minus the 2 synchronization bits) is 10 x TCLK.

In the cable test setup (**Figure 2**), the serializer and deserializer on evaluation (EV) board 2 convert the serial I/O of the Agilent 86130A BER tester to parallel I/O. The parallel data is applied to and read from cable test EV board 1. The serial data sequence output by the 86130A is 1200 bits long and is generated by taking 1000 bits from a pseudorandom binary sequence (PRBS) of $2^{10}-1$ and inserting 01 synchronization bits every 10 PRBS bits. Insertion of the synchronization bits mimics the bits that are added by a serializer. The deserializer on EV board 2 removes the synchronization bits and presents the PRBS data in parallel to the cable test serializer on EV board 1. The serial data sequence is repeated continuously. The Agilent 81250 generates the required reference clocks (TCLK for the serializer and REFCLK for the deserializer).

The BER was tested using cable lengths of 5ft, 15ft, 30ft, 60ft, and 100ft (Ethernet Category 5E, AWG24, unshielded twisted-pair cable manufactured by General Cable, Inc., part no. 2133629H). Eye-diagram jitter was measured at the deserializer input using a Tektronix TDS784C oscilloscope and Tektronix P6247 1.0GHz differential probe. The delays of the TCLK serializer reference clocks generated by the 81250 were adjusted to meet the serializer-input setup and hold-time requirements listed in the data sheet.

Measurements and results

Tests were conducted separately for the MAX9205/MAX9206 and MAX9207/MAX9208 serializer-deserializer pairs. The serial bit rate generated by the 86130A was 192Mbps to 480Mbps for the MAX9205/MAX9206 and 480Mbps to 720Mbps for the MAX9207/MAX9208.

To quantify eye-diagram signal integrity, two parameters are defined: total jitter (t_{TJ}) and marginal jitter (t_{MJ}). t_{TJ} is the timing jitter width measured at zero-differential

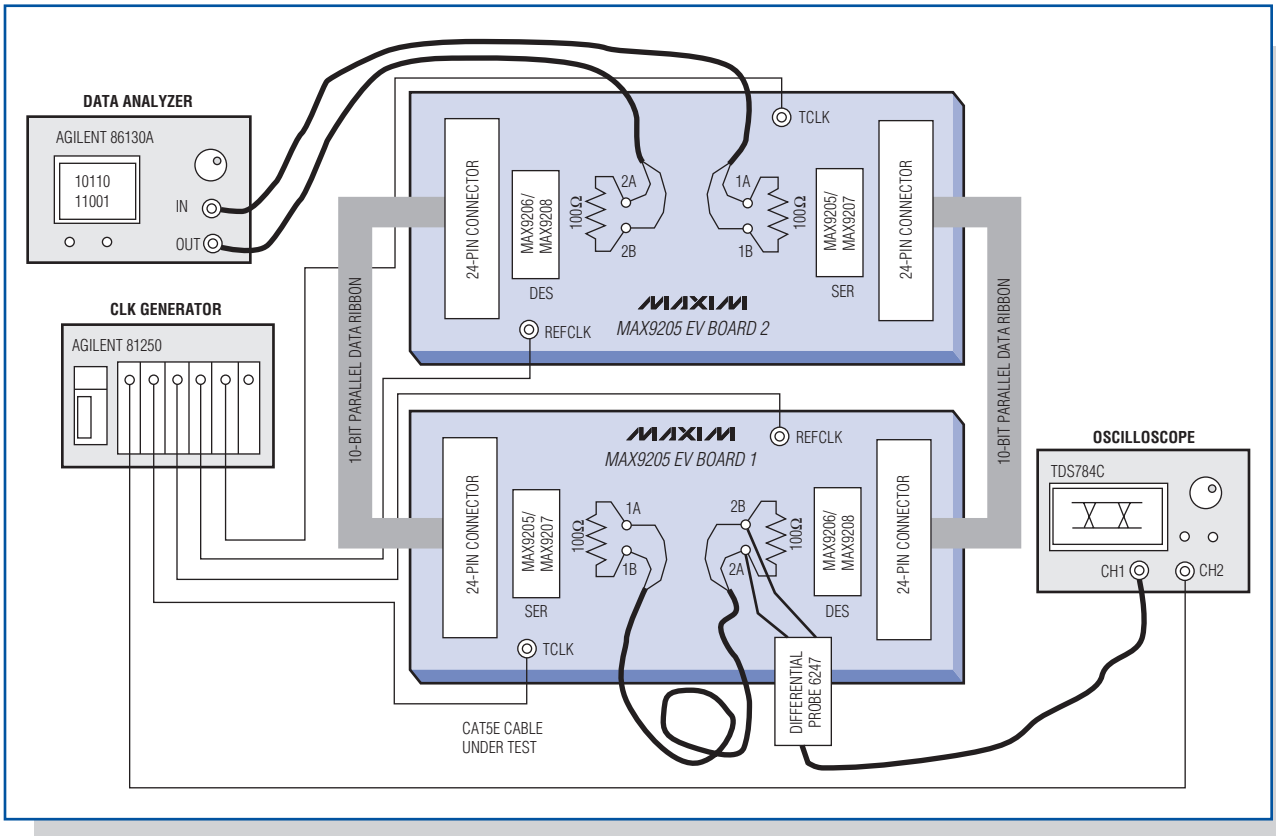

Figure 2. Cable test setup shows the serializer/deserializer which convert the serial I/O to parallel I/O.

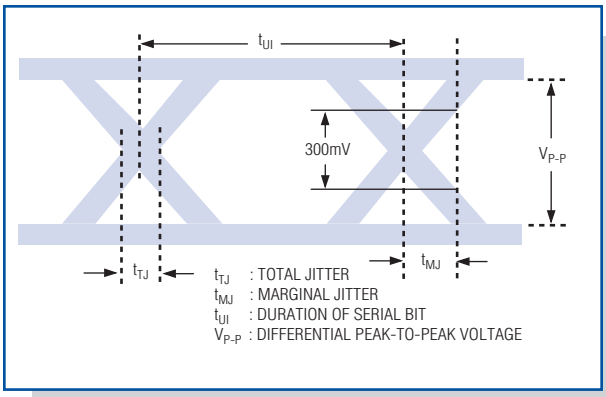

Figure 3. Jitter measurement definitions are used to quantify signal integrity in an eye diagram.

voltage (zero-differential voltage is the main horizontal graticule in the oscilloscope plots). t_{MJ} is the time measured from the center of the jitter at zero-differential voltage to 300mV peak-to-peak differential voltage (**Figure 3**). One might expect the deserializer-differential input to switch at 0V differential, but it is more conservative to assume that additional differential voltage is needed to provide the overdrive. t_{TJ} switches at 0V differential, but t_{MJ} requires the differential signal to reach $300mV_{P-P}$ before it is considered to have switched the deserializer input. Therefore, t_{MJ} is a more conservative measure of signal integrity. t_{UI} (Figure 3) is defined as the duration of a serial bit (unit interval). The unit interval is the period of the reference frequency divided by 12.

The differential peak-to-peak voltage (V_{P-P}) is 2x the difference of the single-ended voltages at the measurement point, or $V_{P-P} = 2 \times |(V_{OUT+}) - (V_{OUT-})|$. For example, at the measurement point, if $V_{OUT+} = 1.35V$ and $V_{OUT-} = 1.10V$ (relative to ground in the high state) and $V_{OUT+} = 1.10V$ and $V_{OUT-} = 1.35V$ (relative to ground in the low state), then $V_{P-P} = 500mV$. Since the measurements are made with a differential probe, which subtracts V_{OUT-} from V_{OUT+}, the eye diagrams show V_{P-P}.

Table 1. MAX9206/MAX9208 maximum marginal jitter

Bit Rate (Mbps)	Data Rate (Mbps)	Maximum Marginal Jitter t_{MJ} (ps)
192	160	1300
480	400	720
720	600	320

Table 1 shows the maximum values of t_{MJ} as specified in the MAX9206/MAX9208 deserializer data sheet. The deserializer is guaranteed to recover data if t_{MJ} is less than or equal to the listed maximum.

Testing was conducted under two conditions. Under the first condition, t_{TJ} and t_{MJ} were measured and bit errors counted while the serial test pattern ran 1hr for each cable length at the highest data rate allowed for the serializer-deserializer pair. Under the second condition, the serial test data was transmitted for more than 10hr (transmitting more than 1.73×10^{13} bits) under high-jitter conditions, that exceeded the maximum data sheet values for t_{MJ}. t_{TJ} and t_{MJ} were measured and bit errors counted.

Tables 2 and **3** show test results for cable lengths from 5ft to 60ft for the MAX9205/MAX9206 and MAX9207/MAX9208 serializer-deserializer pairs. The bit rate is the serial signaling rate and the data rate is the "payload" serial data rate (data rate = (10/12) x bit rate).

Figures 4a and **4b** show eye diagrams taken at the MAX9208 deserializer input after 30ft and 60ft of cable.

To demonstrate the deserializer's capability to recover data under degraded signal conditions (that is, with less jitter margin than specified in the data sheet), tests were conducted for both serializer-deserializer pairs using 100ft of cable. The serial test data was transmitted continuously for more than 10hr. **Table 4** shows the measurements of

Table 2. MAX9205/MAX9206 t_{TJ}, t_{MJ}, V_{P-P}, and bit errors (measured for 1hr)

Cable Length (ft)	Bit Rate (Mbps)	Data Rate (Mbps)	Total Jitter t_{TJ} (ps)*	Marginal Jitter t_{MJ} (ps)*	Differential Voltage V_{P-P} (mV)*	Error Count (1.728×10^{12} bits)
5	480	400	200	220	880	No error
15	480	400	200	260	780	No error
30	480	400	220	320	636	No error
60	480	400	360	560	420	No error

*Measurement resolution for t_{TJ}, t_{MJ} is 10ps. Measurement resolution for V_{P-P} is 2mV.

Table 3. MAX9207/MAX9208 t_{TJ}, t_{MJ},V_{P-P}, and bit errors (measured for 1hr)

Cable Length (ft)	Bit Rate (Mbps)	Data Rate (Mbps)	Total Jitter t_{TJ} (ps)*	Marginal Jitter t_{MJ} (ps)*	Differential Voltage V_{P-P} (mV)*	Error Count (1.728 x 10^{12} bits)
5	720	600	180	200	852	No error
15	720	600	180	230	660	No error
30	720	600	220	270	556	No error
60	720	600	320	N/A (V_{P-P} < 300mV)	292	No error

*Measurement resolution for t_{TJ}, t_{MJ} is 10ps. Measurement resolution for V_{P-P} is 2mV.

Figure 4a

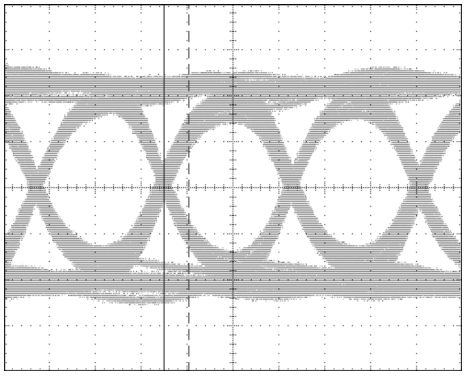

a) 500ps/div

30ft, 720Mbps, t_{TJ} = 220ps, t_{MJ} = 270ps.
2.592 x 10^{12} bits transmitted. No errors.
Vertical scale: 200mV/div.
Horizontal scale: 500ps/div.

Figure 4b

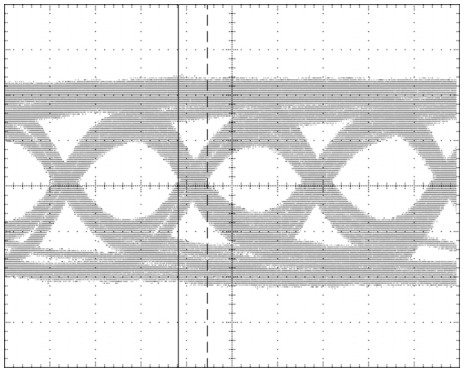

b) 500ps/div

60ft, 720Mbps, t_{TJ} = 320ps, t_{MJ} = N/A.
2.592 x 10^{12} bits transmitted. No errors.
Vertical scale: 200mV/div.
Horizontal scale: 500ps/div.

Figures 4a and 4b. These MAX9208 eye diagrams with 30ft (left) and 60ft (right) cables show the test results for cable lengths from 5ft to 60ft.

jitter, peak-to-peak voltage, and error counts. **Figure 5** provides the eye-diagram plots.

No bit errors are recorded in any of the tests. The amplitude of the signal is 110mV after 100ft of cable at a 520Mbps bit rate, which is approximately one-third the 300mV_{P-P} amplitude specified for t_{MJ}. Also, with t_{TJ} = 1020ps, over half the 1923ps unit interval (t_{UI} = 1/520 Mbps) is jitter. The error-free test result under these conditions provides a measure of the margin in the data sheet specifications (Table 1).

Also, based on the test results, the BER can be predicted. Assume that the probability of error for any bit in the serial data sequence is the same, and the error events are independent among the bits. If the BER is q, then the serial data sequence can be modeled as Bernoulli trials with parameter q. Assuming n is the number of bits transmitted, probability of an n-bit sequence with no error can be expressed as shown in equation 1:

$$P_{no\ error} = (1-q)^n \qquad \text{(Eq 1)}$$

With 100ft of cable, more than 1.73 x 10^{13} were transmitted with no errors. Assuming that the BER value q is less than 3.0 x 10^{-13}, then $P_{no\ error}$ given by equation 1 is 0.0056. This can be interpreted as if the BER has a value of 3.0 x 10^{-13} or bigger; the probability of no error occurring for an observed bit sequence of 1.73 x 10^{13} is 0.0056. Statistically, if a sequence of 1.73 x 10^{13} bits is transmitted without error, the hypothesis of BER < 3.0 x 10^{-13} is 99.44% correct. Since this confidence is obtained with 100ft of cable and poor signal quality, shorter cable lengths and better signal quality increase confidence in the link reliability.

Table 4. MAX9205/MAX9206 and MAX9207/MAX9208 t_{TJ}, t_{MJ},V_{P-P}, and bit errors

Cable Length (ft)	Bit Rate (Mbps)	Data Rate (Mbps)	Total Jitter t_{TJ} (ps)*	Marginal Jitter t_{MJ} (ps)*	Differential Voltage V_{P-P} (mV)*	Conditions
MAX9205/MAX9206						
100	480	400	660	N/A	192	Transmitted bits: 1.73×10^{13} Error bits: 0 Test time: >10hr
MAX9207/MAX9208						
100	520	433	1020	N/A	110	Transmitted bits: 1.87×10^{13} Error bits: 0 Test time: >10hr

*Measurement resolution for t_{TJ}, t_{MJ} is 20ps. Measurement resolution for V_{P-P} is 2mV.

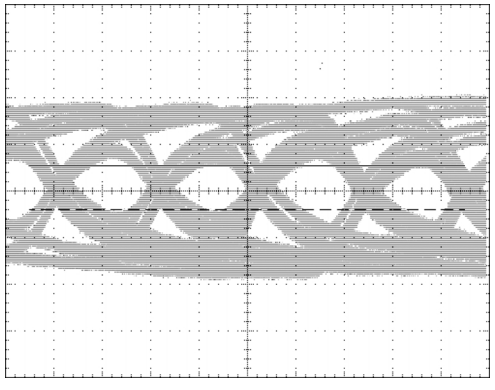

100ns/div

100ft, 480Mbps, t_{TJ} = 660ps, t_{MJ} = N/A.
1.73 ¥ 10^{13} bits transmitted. No errors.
Vertical scale: 200mV/div.
Horizontal scale: 1ns/div.

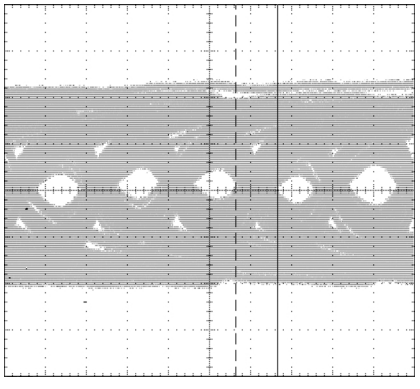

1ns/div

100ft, 520Mbps, t_{TJ} = 1020ps, t_{MJ} = N/A.
1.88 ¥ 10^{13} bits transmitted. No errors.
Vertical scale: 200mV/div.
Horizontal scale: 1ns/div.

Figure 5. These MAX9207/MAX9208 eye diagrams with 100ft cables show different data rates.

Conclusion

Using the BER test, this article has examined the reliability of MAX9205/MAX9206 and MAX9207/MAX9208 serializer-deserializer pairs over low-cost CAT-5E cables of various lengths. The results show that even with severe signal degradation, the link BER is less than 3.0×10^{-13} with more than 99% confidence. The results also demonstrate that the data sheet's maximum jitter limits are sufficient and conservative for high link reliability. Since the measurements were conducted under typical conditions, it is recommended that the criteria in Table 1 be used for real applications. This provides margin to compensate for variations in fabrication, supply voltage, and temperature.

Low-noise amplifier (LNA) matching techniques for optimizing noise figures

An RF amplifier is an active network that increases the amplitude of weak signals, thereby allowing further processing by the receiver. Receiver amplification is distributed between RF and IF stages throughout the system, and an ideal amplifier increases the desired signal amplitude without adding distortion or noise. Unfortunately, amplifiers are known to add noise and distortion to the desired signal. In a receiver chain, the first amplifier after the antenna contributes most to the system noise figure. Adding gain in front of a noisy network reduces the noise contribution from that network.

Amplifier noise figure

To analyze the effect of circuit noise, one can model the noisy circuit as a noiseless circuit plus external noise sources. For a noisy, two-port network with internal noise sources (**Figure 1a**), the effects of those sources are represented by the external noise-voltage sources V_{n1} and V_{n2}, placed in series with the input and output terminals, respectively (**Figure 1b**). Those sources must produce the same noise voltage at the circuit terminals as the internal noise sources. The values of V_{n1} and V_{n2} are calculated in equations 1 and 2. Representing the noise-free, two-port network in Figure 1b by its Z parameters:

$$V_1 = Z_{11}I_1 + Z_{12}I_2 + V_{n1} \quad \text{(Eq 1)}$$

and:

$$V_2 = Z_{21}I_1 + Z_{22}I_2 + V_{n2} \quad \text{(Eq 2)}$$

Equations 1 and 2 show that the V_{n1} and V_{n2} values can be determined from open-circuit measurements in the noisy two-port network. It follows from these equations that when the input and output terminals are open ($I_1 = I_2 = 0$) (equations 3 and 4):

$$V_{n1} = V_1|I_1 = I_2 = 0 \quad \text{(Eq 3)}$$

and:

$$V_{n2} = V_2|I_1 = I_2 = 0 \quad \text{(Eq 4)}$$

In other words, V_{n1} and V_{n2} equal the corresponding open-circuit voltages.

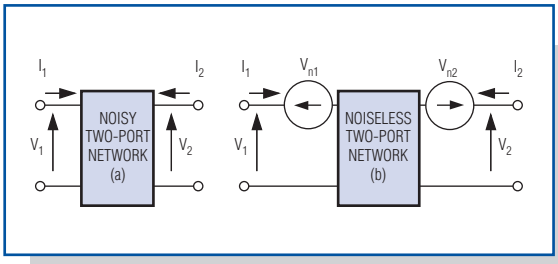

Figure 1. A noisy two-port network (a) can be modeled by a noise-free two-port network (b) with external noise-voltage sources V_{n1} and V_{n2}.

In an alternate representation of the noisy two-port network (**Figure 2**), the external sources are the current-noise sources I_{n1} and I_{n2}. Equations 5 and 6 represent the noise-free two-port network:

$$I_1 = Y_{11}I_1 + Y_{12}I_2 + I_{n1} \quad \text{(Eq 5)}$$

and:

$$I_2 = Y_{21}I_1 + Y_{22}I_2 + I_{n2} \quad \text{(Eq 6)}$$

The values of I_{n1} and I_{n2} in Figure 2 follow from short-circuit measurements taken in the noisy two-port network, as shown in equations 7 and 8:

$$I_{n1} = I_1|V_1 = V_2 = 0 \quad \text{(Eq 7)}$$

and:

$$I_{n2} = I_2|V_1 = V_2 = 0 \quad \text{(Eq 8)}$$

Other representations, besides those shown in Figures 1b and 2, can be derived for a noisy, two-port network. A convenient representation for noise analysis places the noise source at the input of the network (**Figure 3**).

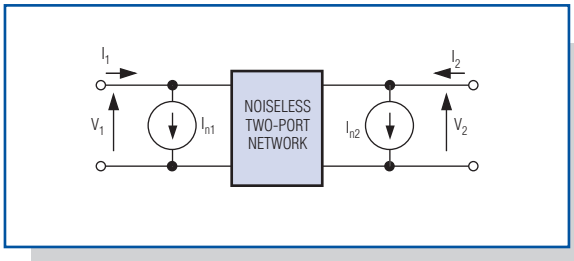

Figure 2. A noisy two-port network can also be represented by a noise-free, two-port network with external noise-current sources I_{n1} and I_{n2}.

Representing the noise-free, two-port network in Figure 3 by its ABCD parameters in equations 9 and 10 show:

$$V_1 = AV_2 + B(-I_2) + V_n \quad \text{(Eq 9)}$$

and:

$$I_1 = CV_2 + D(-I_2) + I_n \quad \text{(Eq 10)}$$

Equations 9 and 10 show that there is no simple way to evaluate V_n and I_n in Figure 3, using open- and short-circuit measurements. From a practical point of view,

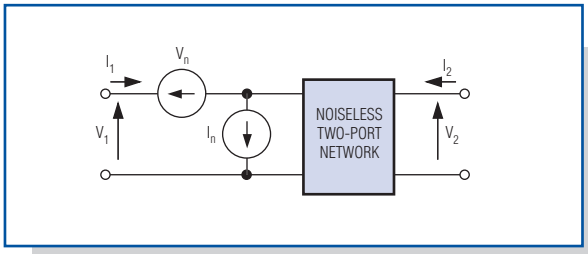

Figure 3. Again, a noisy, two-port network can be represented as a noise-free, two-port network with external noise sources V_n and I_n at the input.

those values (V_n and I_n) can be expressed in terms of noise voltages V_{n1} and V_{n2} in Figure 1b (which require only open-circuit measurements). The relationship between noise sources V_n and I_n in Figure 3 and noise sources V_{n1} and V_{n2} in Figure 1b is derived as follows. Using Z parameters to represent the noise-free, two-port network in Figure 3:

$$V_1 = Z_{11}(I_1 - I_n) + Z_{12}I_2 + V_n = Z_{11}I_1 + Z_{12}I_2 + (V_n - Z_{11}I_n) \quad \text{(Eq 11)}$$

and:

$$V_2 = Z_{21}(I_1 - I_n) + Z_{22}I_2 = Z_{21}I_1 + Z_{22}I_2 - Z_{21}I_n) \quad \text{(Eq 12)}$$

Comparing equations 1 and 2 with equations 11 and 12, it follows that:

$$V_{n1} = V_n - Z_{11}I_n \quad \text{(Eq 13)}$$

and:

$$V_{n2} = -Z_{21}I_n \quad \text{(Eq 14)}$$

Hence, solving equations 13 and 14 for V_n and I_n gives:

$$V_n = V_{n1} - \left(\frac{Z_{11}}{Z_{21}}\right)I_{n2} \quad \text{(Eq 15)}$$

and:

$$I_n = -\left(\frac{V_{n2}}{Z_{21}}\right) \quad \text{(Eq 16)}$$

An alternate method for determining V_n and I_n relates them to noise sources I_{n1} and I_{n2} in Figure 2. It is easy to show that the relations in this case are:

$$V_n = -\left(\frac{I_{n2}}{Y_{21}}\right) \quad \text{(Eq 17)}$$

and:

$$I_n = I_{n1} - \left(\frac{Y_{11}}{Y_{21}}\right)I_{n2} \quad \text{(Eq 18)}$$

A source connected to the noisy two-port network (**Figure 4**) is represented by a current source with admittance Y_s. It is assumed that noise from the source is uncorrelated with noise from the two-port network. Thus, noise power is proportional to the mean square of the short-circuit current (denoted by $\overline{I^2_{SC}}$) at the input port of the noise-free amplifier; and noise power due to the source alone is proportional to the mean square of the source current ($\overline{I^2_S}$). Hence, the noise figure F is given by:

$$F = \frac{\overline{I^2_{SC}}}{\overline{I^2_S}} \quad \text{(Eq 19)}$$

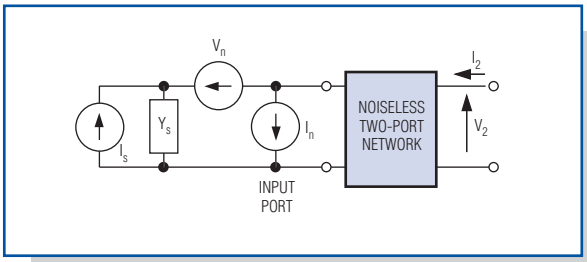

Figure 4. This noise model lets you calculate the amplifier noise figure.

Because $I_{sc} = -I_s + I_n + V_nY_s$, it follows that the mean square of I_{sc} is given by equation 20:

$$\overline{I^2_{sc}} = \left(\overline{-I_s + I_n + V_nY_s}\right)^2 = \overline{I^2_s} + \left(\overline{I_n + V_nY_s}\right)^2 - 2\overline{I_s}\left(\overline{I_n + V_nY_s}\right) \quad \text{(Eq 20)}$$

Because noise from the source and noise from the two-port network are uncorrelated:

$$\overline{I_s}\left(\overline{I_n + V_nY_s}\right) = 0 \quad \text{(Eq 21)}$$

and equation 20 reduces to:

$$\overline{I^2_{sc}} = \overline{I^2_s} + \left(\overline{I_n + V_nY_s}\right)^2 \quad \text{(Eq 22)}$$

Substituting equation 20 into equation 19 gives:

$$F = 1 + \frac{\left(\overline{I_n + V_nY_s}\right)^2}{\overline{I^2_s}} \quad \text{(Eq 23)}$$

There is some correlation between external sources V_n and I_n. Hence, I_n can be written as the sum of two terms—one uncorrelated to V_n (I_{un}) and one correlated to V_n (I_{nc}). Thus:

$$I_n = I_{nu} + I_{nc} \qquad \text{(Eq 24)}$$

Furthermore, the relation between I_{nc} and V_n in terms of a correlation admittance Y_c is defined as:

$$I_{nc} = Y_c V_n \qquad \text{(Eq 25)}$$

Y_C is not an actual admittance in the circuit; it is defined by equation 25 and calculated as follows. From equation 24:

$$I_n = I_{nu} + Y_c V_n \qquad \text{(Eq 26)}$$

Multiplying equation 26 by V x $_n$, taking the mean, and observing that $\overline{I_{nu} V_n^*} = 0$:

$$\overline{I_n V_n^*} = Y_c \overline{V^2_n} \quad \text{or} \quad Y_c = \frac{\overline{V^*_n I_n}}{\overline{V^2_n}} \qquad \text{(Eq 27)}$$

Substituting equation 26 into equation 23 produces the following expression for F:

$$F = 1 + \frac{\left(\overline{I_{nu} + (Y_c + Y_s)V_n}\right)^2}{\overline{I^2_s}} \qquad \text{(Eq 28)}$$

Noise produced by the source is related to the source conductance by:

$$\overline{I^2_s} = 4kT_0 G_s B \qquad \text{(Eq 29)}$$

where $G_s = \mathrm{Re}[Y_s]$. The noise voltage can be expressed in terms of an equivalent noise resistance R_n as:

$$\overline{V^2_n} = 4kT_0 R_n B \qquad \text{(Eq 30)}$$

and the uncorrelated noise current can be expressed in terms of an equivalent noise conductance G_u:

$$\overline{I^2_{nu}} = 4kT_0 G_u B \qquad \text{(Eq 31)}$$

Substituting equations 29, 30, and 31 into equation 28, and letting:

$$Y_c = G_c + jB_c \qquad \text{(Eq 32)}$$

and:

$$Y_s = G_s + jB_s \qquad \text{(Eq 33)}$$

gives:

$$F = 1 + \frac{4kT_0 G_u B + \left|G_s + jB_s + G_c + jB_c\right|^2 4kT_0 R_n B}{4kT_0 G_s B} =$$

$$1 + \frac{G_u}{G_s} + \frac{R_n}{G_s}\left[(G_s + G_c)^2 + (B_s + B_c)^2\right] \qquad \text{(Eq 34)}$$

The noise factor can be minimized by properly selecting Y_S. From equation 34, F is decreased by selecting:

$$B_s = -B_c \qquad \text{(Eq 35)}$$

Hence, from equation 34:

$$F_{Bs=-Bc} = 1 + \frac{G_u}{G_s} + \frac{R_n}{G_s}(G_s + G_c)^2 \qquad \text{(Eq 36)}$$

The dependence of the expression in equation 34 on G_s can be minimized by setting:

$$\frac{F_{Bs=-Bc}}{dG_s} = 0' \qquad \text{(Eq 37)}$$

This gives:

$$\frac{F_{Bs=-Bc}}{dG_s} = -\frac{G_u}{G^2_s} + R_n \frac{\left(2G_s(G_s + G_c) - (G_s + G_c)^2\right)}{G^2_s} = 0$$

(Eq 38)

Solving for G_S:

$$G_s = \sqrt{G^2_c + \frac{G_u}{R_n}} \qquad \text{(Eq 39)}$$

The values of G_S and B_S in equations 39 and 35 give the source admittance, which results in the minimum (optimum) noise figure. This optimum value of the source admittance is commonly denoted by $Y_{opt} = G^{opt} + jB_{opt}$; that is:

$$Y_{opt} = G_{opt} + jB_{opt} = \sqrt{G^2_c + \frac{G_u}{R_n}} - jB_c \qquad \text{(Eq 40)}$$

From equation 36, the minimum noise figure F_{min} is:

$$F_{min} = F\Big|_{Y_S = Y_{opt}} = 1 + \frac{G_u}{G_{opt}} + \frac{R_n}{G_{opt}}\left(G_{opt} + G_c\right)^2$$

(Eq 41)

Solving equation 39 for G_u/G_{opt} and substituting into equation 41 gives:

$$F_{min} =$$

$$1 + R_n\left(G_{opt} - \frac{G^2_c}{G_{opt}}\right) + \frac{R_n}{G_{opt}}\left(G^2_{opt} + 2G_{opt}G_c + G^2_c\right) =$$

$$1 + 2R_n\left(G_{opt} + G_c\right) \qquad \text{(Eq 42)}$$

Using equation 42, equation 34 can be expressed as:

$$F = F_{min} - 2R_n\left(G_c + G_{opt}\right) + \frac{G_u}{G_s} +$$

$$- \frac{R_n}{G_s}\left[\left(G_s + G_c\right)^2 + \left(B_s - B_{opt}\right)^2\right] \qquad \text{(Eq 43)}$$

Solving equation 39 for G_U and substituting into equation 43, the expression for F can be simplified:

$$F = F_{min} + \frac{R_n}{G_s}\left[\left(G_s - G_{opt}\right)^2 + \left(B_s - B_{opt}\right)^2\right] \quad \text{(Eq 44)}$$

Equation 44 shows that F depends on $Y_{opt} = G_{opt} + jB_{opt}$, and on F_{min}. When these quantities are specified, the value of noise figure F can be determined for any source admittance Y_s. This equation can also be expressed as:

$$F = F_{min} + \frac{R_n}{G_s}\left|y_s - y_{opt}\right|^2 = F_{min} + \frac{R_n}{Real(y_s)}\left|Y_s - Y_{opt}\right|^2 \quad \text{(Eq 45)}$$

where $rn = R_n/Z_0$ is the normalized noise resistance and $y_s = Y_S Z_0$ is the normalized source admittance:

$$y_s = \frac{Y_s}{Y_0} = \frac{G_s + jB_s}{Y_0} = g_s + jb_s \quad \text{(Eq 46)}$$

y_{opt} is the normalized value of the optimum source admittance:

$$y_{opt} = \frac{Y_{opt}}{Y_0} = \frac{G_{opt} + jB_{opt}}{Y_0} = g_{opt} + jb_{opt} \quad \text{(Eq 47)}$$

Admittances y_s and y_{opt} can be expressed in terms of reflection coefficients:

$$y_s = \frac{1-\Gamma_s}{1+\Gamma_s} \longleftrightarrow \Gamma_s = \frac{1-y_s}{1+y_s}$$

and

$$y_{opt} = \frac{1-\Gamma_{opt}}{1+\Gamma_{opt}} \longleftrightarrow \Gamma_{opt} = \frac{1-y_{opt}}{1+y_{opt}} \quad \text{(Eq 48)}$$

Expressing y_s and y_{opt} in terms of reflection coefficients helps formulate the noise figure (equation 45) as a function of those coefficients. This formulation is more convenient for industrial LNA applications because in most data sheets, the LNA characteristics are expressed as a table of S parameters and the optimum reflection coefficient G_{opt} vs. frequency:

$$F = F_{min} + 4r_n \frac{\left|\Gamma_s - \Gamma_{opt}\right|^2}{\left|1+\Gamma_{opt}\right|^2\left(1-\left|\Gamma_s\right|^2\right)} \quad \text{(Eq 49)}$$

When the noise figure (F in equation 46) is expressed as a function of a circle, it can be used with a Smith chart for optimum noise-figure matching in specific applications:

$$\frac{F - F_{min}}{4r_n}\left|1+\Gamma_{opt}\right|^2 = \frac{\left|\Gamma_s - \Gamma_{opt}\right|^2}{\left(1-\left|\Gamma_s\right|^2\right)}$$

$$N = \frac{\left|\Gamma_s - \Gamma_{opt}\right|^2}{\left(1-\left|\Gamma_s\right|^2\right)} \quad \text{with} \quad N = \frac{F - F_{min}}{4r_n}\left|1+\Gamma_{opt}\right|^2$$

$$N = \frac{\left|\Gamma_s\right|^2 - 2\Gamma_s\Gamma_{opt} + \left|\Gamma_{opt}\right|^2}{\left(1-\left|\Gamma_s\right|^2\right)}$$

$$N\left(1-\left|\Gamma_s\right|^2\right) = \left|\Gamma_s\right|^2 - 2\Gamma_s\Gamma_{opt} + \left|\Gamma_{opt}\right|^2$$

$$(1+N)\left|\Gamma_s\right|^2 = N + 2\Gamma_s\Gamma_{opt} - \left|\Gamma_{opt}\right|^2$$

$$\left|\Gamma_s\right|^2 = \frac{N}{(1+N)} + \frac{2\Gamma_s\Gamma_{opt}}{(1+N)} - \frac{\left|\Gamma_{opt}\right|^2}{(1+N)}$$

$$\left|\Gamma_s\right|^2 - \frac{2\Gamma_s\Gamma_{opt}}{(1+N)} + \frac{\left|\Gamma_{opt}\right|^2}{(1+N)^2} - \frac{\left|\Gamma_{opt}\right|^2}{(1+N)^2} = \frac{N}{(1+N)} - \frac{\left|\Gamma_{opt}\right|^2}{(1+N)}$$

$$\left|\Gamma_s - \frac{\Gamma_{opt}}{(1+N)}\right|^2 = \frac{1}{(1+N)^2}\left[N^2 + N\left(1-\left|\Gamma_{opt}\right|^2\right)\right]$$

(Eq 50)

For LNA input matching, a noise circle is positioned on the Smith chart as follows:

$$\text{Center: } O_N = \frac{\Gamma_{opt}}{(1+N)} \quad \text{with} \quad N = \frac{F - F_{min}}{4r_n}\left|1+\Gamma_{opt}\right|^2 \quad \text{(Eq 51)}$$

$$\text{Radius: } R_N = \frac{1}{(1+N)}\sqrt{\left[N^2 + N\left(1-\left|\Gamma_{opt}\right|^2\right)\right]} \quad \text{(Eq 52)}$$

From equations 51 and 52, one can visualize the noise performance of an LNA by plotting the noise circles on the Smith chart. This technique allows the designer to see the effect of tuning in order to estimate the practical noise performance.

Designing for optimum noise figure

For any two-port network, the noise figure measures the amount of noise added to a signal transmitted through the network. For any practical circuit, the signal-to-noise ratio (SNR) at its output is worse (smaller) than at its input. In most circuit designs, however, the noise contribution of each two-port network can be minimized through a judicious choice of operating point and source resistance.

The preceding section demonstrates that for each LNA (indeed, for any two-port network), there exists an optimum noise figure. LNA manufacturers often specify an optimum source resistance in the data sheet. As an alternative, data sheets for the MAX2656 and other LNAs specify an optimum source-reflection coefficient.

To design an amplifier for minimum noise figure, determine (experimentally or from the data sheet) the source resistance and bias point that produce the minimum noise figure for that device. Then force the actual source impedance to "look like" that optimum value with all stability considerations still applying. If the Rollet stability factor (K) is calculated to be less than 1 (K is defined as a figure of merit for LNA stability), then you must be careful in choosing the source and load-reflection coefficients. For an accurate depiction of the unstable regions, it is best to draw stability circles.

After providing the LNA with optimum source impedance, the next step is to determine the optimum load-reflection coefficient (Γ_L) needed to properly terminate the LNA's output:

$$\Gamma_L = \left[S_{22} + \frac{S_{21}\Gamma_S S_{12}}{1 - S_{11}\Gamma_S} \right]^*, \qquad \text{(Eq 53)}$$

where Γ_S is the source-reflection coefficient necessary for minimum noise figure. (The asterisk in the above equation indicates the conjugate of the complex quantity Γ_L.)

Applications

A practical example to illustrate the theory of optimum noise matching for LNAs is the MAX2656—an LNA (**Figure 5**) with high third-order adjustable intercept point (IP3). Designed for PCS phone applications with gain selected by logic control (14.5dB in high-gain mode and 0.8dB in low-gain mode), the amplifier exhibits an optimum noise figure of 1.9dB (depending on the value of bias resistor R_{BIAS}). The MAX2655/MAX2656 IP3 is adjusted with a single external bias resistor (R_{BIAS}), which lets you optimize the supply current for specific applications.

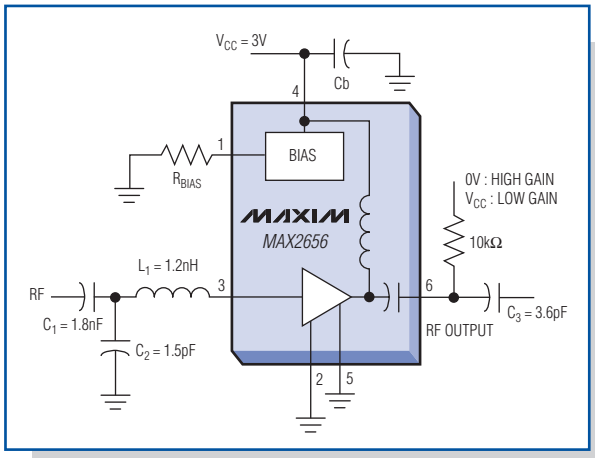

Figure 5. This typical operating circuit for the MAX2656 LNA shows design values for the input-matching network.

Figure 5's application employs a MAX2656 LNA operating at a PCS receiver frequency of 1960MHz and noise figure of 2dB (as requested by design). It must operate between 50Ω terminations. As described in the MAX2656 data sheet, the optimum bias resistance (R_{BIAS}) for minimum noise figure is 715Ω. The optimum source-reflection coefficient Γ_{OPT} for minimum noise figure in a 1960MHz application (F_{MIN} = 1.79dB) is:

$$\Gamma_{opt} = 0.130 / 124.48° \qquad \text{(Eq 54)}$$

A source impedance with noise-equivalent resistance RN = 43.2336Ω yields the minimum noise figure.

A MAX2656 LNA operating at 1960MHz has the following S parameters (expressed as magnitude/angle):

- S11 = 0.588/-118.67°
- S21 = 4.12/149.05°
- S12 = 0.03/-167.86°
- S22 = 0.275/-66.353°

The calculated stability factor (K = 2.684) indicates unconditional stability, so we can proceed with the design. Figure 5 shows design values for the input-matching network. First, a Smith chart for input matching shows (in blue) the 2dB constant-noise circle requested by design (**Figure 6**). For comparison, note the dotted-line depiction of constant-noise circles corresponding to the noise figures of 2.5dB, 3dB, and 3.5dB.

For convenience, we chose a source-reflection coefficient of Γ_S = 0.3/150° on the 2dB constant-noise circle. The normalized 50Ω source resistance is transformed to Γ_S using two components: the arc Γ_SA (clockwise in the impedance chart) gives the value of series inductance L_1. Arc BO (clockwise in the admittance chart) gives the value of shunt capacitor C_1.

The value of arc Γ_SA measured on the plot is 0.3 units, so Z = 50 x 0.3 = 15Ω. Thus, $L_1 = 15/\omega = 15/(2\pi f) = 15/[2\pi \times (1.96 \times 10^9)] = 1.218$nH, rounded to 1.2nH. The value of the arc BO measured on the plot is 0.9 units, so $1/Y = Z = 50/0.9 = 55.55\Omega$. Thus, $C_2 = 1/(55.55 \times \omega) = 1/(55.55 \times 2\pi f) = 1/[55.55 \times 2\pi \times (1.96 \times 10^9)] = 1.46$pF, rounded to 1.5pF.

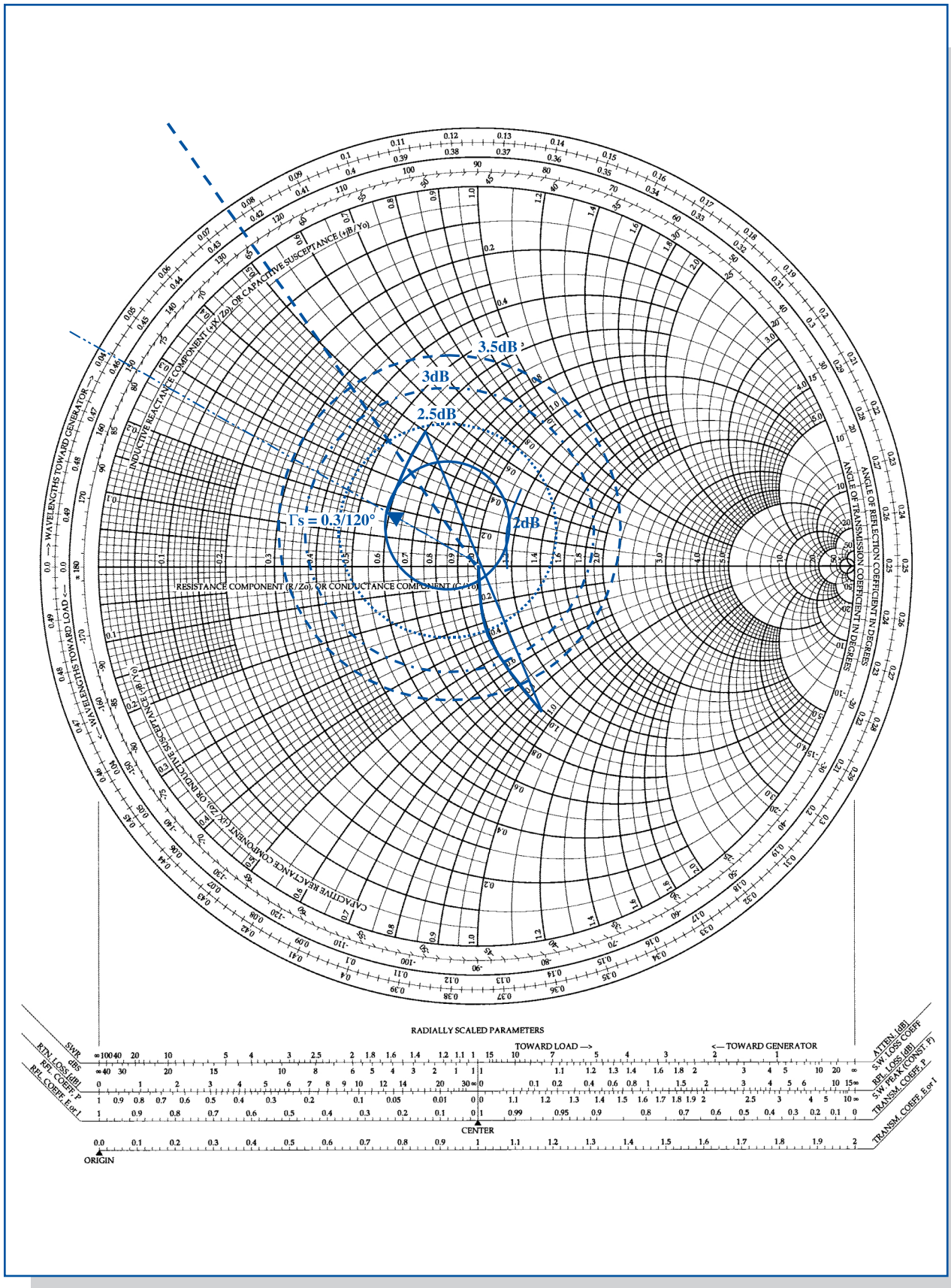

Figure 6. The solid circle on this Smith chart depicts the desired (optimum) 2dB noise figure for a MAX2656 PCS LNA with input matching.

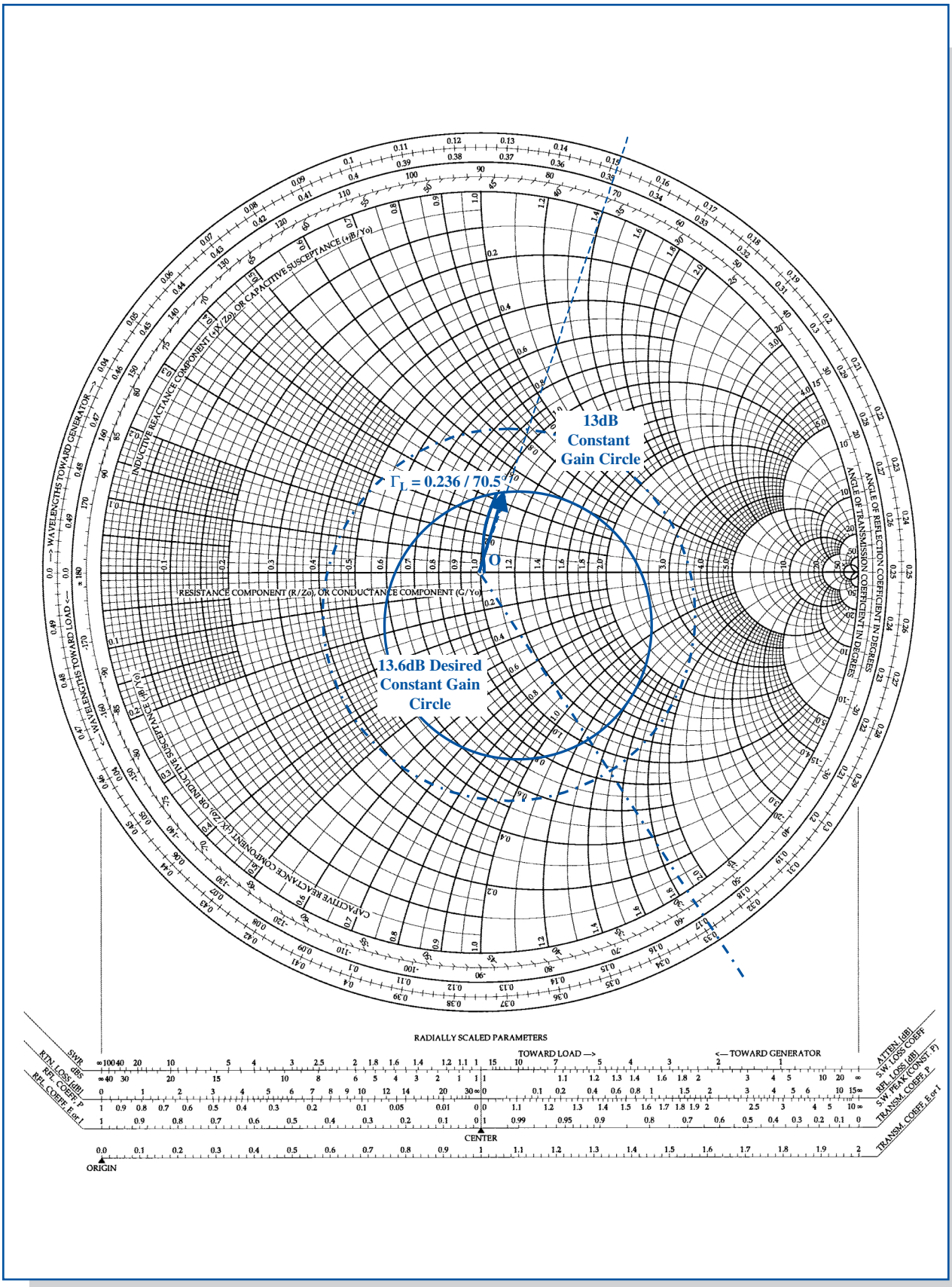

Figure 7. The MAX2656 PCS LNA has output matching for a desired (optimum) 2dB noise figure.

C_1 is simply a high-valued DC-isolation capacitor and does not interfere with the input matching. The chosen Γ_S provides the load-reflection coefficient needed to properly terminate the LNA:

$$\Gamma_L = \left[S_{22} + \frac{S_{21}\Gamma_s S_{12}}{1 - S_{11}\Gamma_s} \right]^* = 0.236 / 70.5° \qquad \text{(Eq 55)}$$

This value and the normalized load-resistance value are plotted in **Figure 7**, which also shows a possible method for transforming the 50Ω load into Γ_L. For this example, note that a single series capacitor provides the necessary impedance transformation.

The arc $O\Gamma_L$ (counterclockwise in the impedance chart) gives the value for series capacitor C_3. The value of arc $O\Gamma_L$ measured on the plot is 0.45 units, so Z = 50 x 0.45 = 22.5Ω. Thus, C3 = 1/(22.5 x ω) = 1/(22.5 x 2πf) = 1/[22.5 x 2π x (1.96 x 10^9)] = 3.608pF, rounded to 3.6pF.

Conclusion

These calculations have determined the matching components required for optimum noise performance in the LNA of Figure 5. Of course, in low-cost applications where optimum noise performance is not mandatory, C3 can be omitted, and the MAX2656 can be connected directly to a 50Ω system.

References:

1. Gonzalez, Guillermo; Microwave Transistor Amplifiers, Analysis & Design; Second Edition, Prentice Hall, Upper Saddle River, New Jersey 07458.
2. Bowick, Chris; RF Circuit Designs; Howard W. Sams & Co. Inc., a publishing subsidiary of ITT.